American Mineralogist, Volume 84, pages 1041–1048, 1999

Vibrational analysis of the dioctahedral mica: $2M_1$ muscovite

DAVID A. MCKEOWN,[1,*] MICHAEL I. BELL,[2] AND EDGAR S. ETZ[3]

[1]Vitreous State Laboratory, Catholic University of America, 620 Michigan Avenue, N.E., Washington, D.C. 20064, U.S.A.
[2]Naval Research Laboratory, Dynamics of Solids Branch, Code 6680, Washington, D.C. 20375-5320, U.S.A.
[3]Surface and Microanalysis Science Division, National Institute of Standards and Technology, Gaithersburg, Maryland 20899-0001, U.S.A.

ABSTRACT

Raman spectra and lattice dynamics calculations are presented for the dioctahedral mica, muscovite. Calculated fundamental mode frequencies for the Raman-active and A_g and B_g species were fit to observed fundamentals assigned to features in the two polarized Raman spectra collected, so that unambiguous vibrational assignments could be made to most peaks in the Raman data. Calculated frequencies for the IR-active A_u and B_u modes generally fall within the frequency ranges of bands in the IR spectra for muscovite presented earlier. Factor group analysis indicates that motion from all atom types in the muscovite structure can be found in modes for all four vibrational species. Force constant values determined for muscovite are similar to equivalent values calculated for the trioctahedral mica, phlogopite. Raman and IR-active modes calculated at frequencies greater than 800 cm^{-1} are dominated by internal sheet T-O stretch and T-O-T bend motions, where T is a tetrahedral site. Modes between 800 and 360 cm^{-1} have internal tetrahedral sheet motions mixed with K and octahedral Al displacements. Modes at frequencies less than 360 cm^{-1} have lattice and OH motions. Inter-sheet bonding in the muscovite structure is strong enough to affect modes at frequencies as high as 824 cm^{-1}.

INTRODUCTION

This work describes the Raman spectra and lattice dynamic calculations of the zone-center optical phonons of the dioctahedral mica, $2M_1$ muscovite. The motivation of this work is to provide vibrational assignments to the Raman spectra of sheet silicates. Muscovite has been the subject of IR and Raman studies (Loh 1973; Velde 1978; Haley et al. 1982), but vibrational assignments have not been determined for all observed modes.

The monoclinic *C2/c* crystal structure of $2M_1$ muscovite is comprised of tetrahedral sheets that are bonded together by alternating layers of K^+ and octahedral Al^{+3} (Guven 1971). The atoms in the $2M_1$ muscovite structure are all in general positions, except for K, which has C_2 or 2 symmetry. The sheets contain two tetrahedral sites, T1 and T2 (Fig. 1), where approximately 75% of these sites are randomly occupied by Si, while the remaining 25% contain Al. The sheets are bonded together by K^+ layers and dioctahedral layers, where Al^{+3} occupy the M2 octahedral sites; the M1 octahedral sites are vacant. Each octahedral Al is coordinated by four non-bridging O atoms (O_{nb}), two Oa and two Ob, as well as two OH. The K atoms are coordinated to six bridging O atoms (O_{br}): two Oc, two Od. and two Oe from two adjacent tetrahedral sheets. Each tetrahedral site is coordinated by three O_{br}: one of each of the three O_{br} types, and one O_{nb}: T1 to Oa and T2 to Ob. The tetrahedra link to form six-membered rings that are each connected to six other symmetrically equivalent six-membered rings.

Overall, the atomic arrangement in muscovite is similar to the phlogopite structure, where T in phlogopite is equivalent to T1 and T2, O1 is equivalent to Oc and Oe, O2 is equivalent to Od, and O3 is equivalent to Oa and Ob (McKeown et al. 1999). The most conspicuous differences between the two structures are the unoccupied M1 sites in muscovite, an OH site shift relative to the K site, and an O_{nb} shift relative to the T sites (compare the *z* axis projection in Fig. 1 with Fig. 1 in McKeown et al. 1999).

FACTOR GROUP ANALYSIS

Factor group analysis (FGA) was performed for the muscovite structure (Table 1) using the method of Fateley et al. (1972). In contrast to phlogopite, the lower symmetry muscovite structure imposes vibrational contributions from all atom types to the four vibrational species.

TABLE 1. The irreducible representations of muscovite

	A_g (R)	B_g (R)	A_u (IR)	B_u (IR)
K	1	2	1	2
M2	3	3	3	3
OH	3	3	3	3
T_2O_5	21	21	21	21
N_{total}	28	29	28*	29†

Notes: Contributions are given for K, M2, OH, and T_2O_5 sheets. Species followed by the notation (R) and (IR) are Raman or infrared active, respectively.
* Includes one acoustic mode.
† Includes two acoustic modes.

*E-mail: davidm@rsrch.vsl.cua.edu

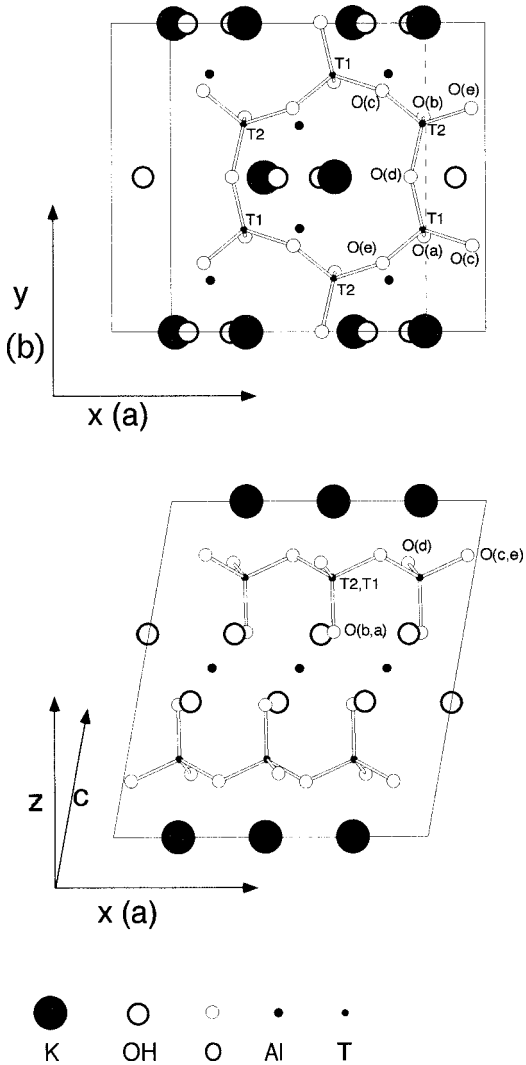

FIGURE 1. The cell of the muscovite structure on which the calculation is based. The *x* and *y* axes used in the calculations are parallel to the *a* and *b* axes, respectively, of the crystal structure. The calculations used cartesian coordinates and an orthogonal coordinate system, hence the *z* axis is not coincident to the *c* axis of the monoclinic crystal structure. The top view is the *z* axis projection, where only the top tetrahedral sheet is shown for clarity. The bottom view is the *y* axis projection. All T-O bonds as well as the T and oxygen labeling conventions are indicated.

EXPERIMENTAL METHODS

The muscovite sample used in this study is a clear plate approximately 5 cm × 7 cm × 1 mm that was collected at the Amphlett Mine, Cherokee County, Georgia (sample no. 105100, supplied by the Mineral Sciences Department, National Museum of Natural History, Smithsonian Institution). The sample used here was refined by Guven (1973) and has the chemical formula: $[K_{0.86}Na_{0.10}(H_3O)^{+}_{0.01}][(Al_{1.90}Ti_{0.01}Fe^{+3}_{0.02}Fe^{++}_{0.05}Mg_{0.06})(Si_{3.02}Al_{0.98})O_{10.08}(OH)_{1.92}]$.

Polarized single-crystal Raman spectra were obtained from the oriented single crystal in backscattering geometry using a Bruker FT-Raman instrument (Model RFS-100). The source was a Nd:YAG laser supplying 1.064 μm wavelength excitation at 600 mW. Variable power densities were initially placed at the sample to make sure that no sample modification was incurred. The detection system consisted of a high-sensitivity germanium detector operated at liquid nitrogen temperature. All spectra were recorded at 4 cm^{-1} resolution and were corrected for the instrument response function. Raman shift calibration ensured that band frequency positions are accurate to within 1 cm^{-1}. In each scattering geometry, the FT-Raman spectrum was acquired through 640 coadded scans to optimize signal-to-noise. Using near-IR excitation eliminated any laser induced luminescence from the sample.

The flat surface of the crystal was oriented perpendicular with respect to the incident and the scattered light propagation directions. The procedure for determining the vibrational species contributing to each polarized Raman spectrum is outlined in Loudon (1964). The Raman spectra (Fig. 2) are similar to preliminary micro-Raman data collected on the same muscovite sample as well as the spectra for green muscovite in Loh (1973). The micro-Raman spectra are not presented, because laser light-scattering masked all features below 240 cm^{-1} for A_g and below 150 cm^{-1} for B_g. At frequencies above the low frequency micro-Raman limits, observed spectral features are reproducible among all data collected for the Georgia muscovite sample. Raman spectral features at frequencies greater than 800 cm^{-1} in Figure 2 are not clearly observable in Loh's spectra. Intensity differences are found for the prominent peak near 106 cm^{-1} in Loh's study and the relatively small peak near 101 cm^{-1} in our B_g spectrum (Fig. 2b). Raman-active mode frequencies listed by Loh at 106, 163, 198, and 265 cm^{-1} correspond to our observed 198 cm^{-1} A_g mode and B_g modes at 106, 173, and 265 cm^{-1}. Haley et al. (1982) list vibrational mode frequencies above 650 cm^{-1}, where the 673, 703, 752, 801, 809, 851, 910, 916, 967, 1019, 1091, and 1120 cm^{-1} modes appear to correspond to our observed A_g modes at 703, 754, 800, 811, 913, 958, 1024, 1098, and 1116 cm^{-1}, and to our observed B_g modes at 669, 704, 754, 804, 851, 912, 954, 1017, 1098, and 1116 cm^{-1}.

NORMAL COORDINATE ANALYSIS

An arrangement of 74 atoms representing the muscovite structure was used in the lattice dynamics calculations at zero wavevector, following the procedure reported earlier (Kim et al. 1993). A total of 132 bond stretching and bending interactions were defined in the calculations, which adequately described the bonding environments in the muscovite structure so that all calculated fundamental optical modes have non-zero frequencies.

Several sites in the muscovite structure are occupied by more than one atom type. The K and M2 sites are dominated by K and Al, respectively; and therefore, K and Al masses were used for those sites in the calculations. The mass used for the two T sites was a weighted average of Si and Al, reflecting the site occupancy described above.

Initial calculations used force constant values similar to those determined for phlogopite. Eight force constants were adjusted

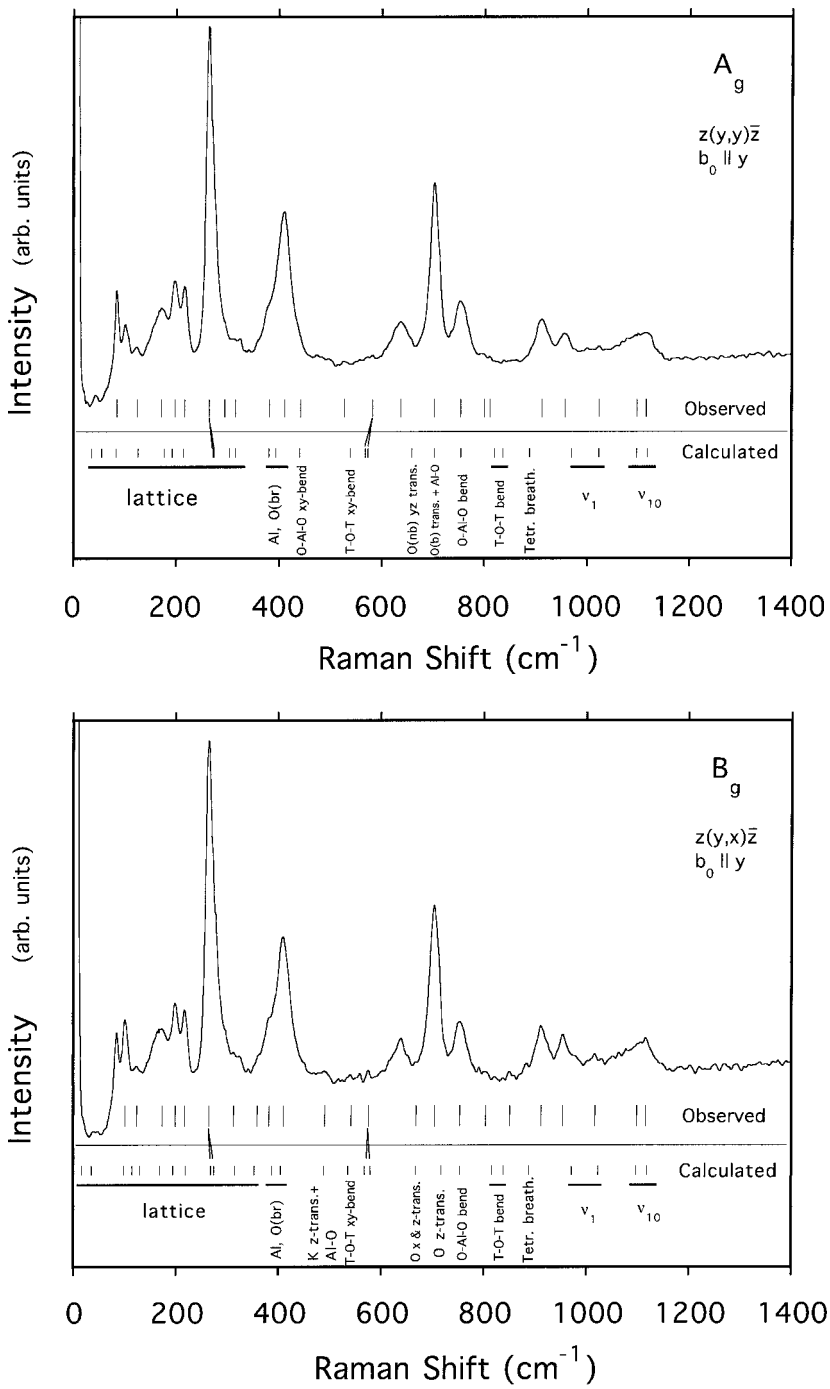

FIGURE 2. The Raman spectrum of **(a)** A_g and **(b)** B_g symmetry for muscovite. Below, fundamental frequencies for **(a)** A_g and **(b)** B_g are indicated as vertical bars. Labeled as calculated are the theoretical frequencies plotted as short vertical bars and vibrational assignments from the normal coordinate analysis. The spectra were collected with **(a)** incident and scattered light polarized parallel to [010] and **(b)** incident light polarized parallel to [010] and scattered light polarized parallel to [100]. Porto's notation for polarization is indicated. See axis labels in Figure 1.

to give the best fit of the calculated frequencies to the observed mode frequencies in the two Raman spectra (Table 2). The fitting was accomplished by minimizing the root-mean-square (rms) deviation between calculated and observed fundamental frequencies (Kim et al. 1993). The initial rms (near 20 cm^{-1}) quickly converged to a final value of 9.9 cm^{-1}.

In most cases, mode frequencies determined from the spectral features provided guidelines and constraints for the calculated frequencies. In some instances, the calculated frequencies

TABLE 2. Force constant values determined for muscovite

Force constant	Interaction	Value
k_1	T-O_{nb}	4.11×10^5 dyne/cm
k_2	T-O_{br}	4.56
k_3	M2-O	2.44
k_4	M2-OH	0.58
k_5	K-O	1.59
k_6	O_{nb}-T-O_{br}	0.63×10^{-11} erg
k_7	O_{br}-T-O_{br}	1.03
k_8	M2-O_{nb}-T	0.38

Notes: These produce an rms deviation of 9.9 cm^{-1}.

TABLE 3. Raman-active A_g $z(y,y)\bar{z}$ mode frequencies and assignments for muscovite

Observed (cm^{-1})	Calculated (cm^{-1})	Assignment
–	1	OH *xz*-trans.
–	36	sheet + K *x*-trans. shearing M2 environment
–	55	sheet *xz*-trans. + OH-M2-OH bend
85	83	Sheet *yz*-trans. + K *y*-trans.
124	126	Sheet *xz*-trans. + K *xy*-trans. (minor)
172	177	M2-OH stretch (M2 *z*-trans.)
198	193	M2-OH stretch + Od *xz*-trans.
217	214	OH-M2-OH bend + M2-Oa stretch
265	272	Ob, OH *y*-trans. + Oc,e *z*-trans. + K *y*-trans.
265	274	T1-Oa *z*-trans. + T2-Ob -*z*-trans. + M2 *xy*-trans. + K *xy*-trans.
295	304	M2-OH stretch + M2-Oa stretch
316	315	M2-OH stretch + M2-Ob stretch + tetrahedral rot. || *z*
382	380	M2 *z*-trans. + Oc *z*-trans. + Od,e -*z*-trans.
411	394	M2 *xz*-trans. +Od *z*-trans. + Oc,e *xz*-trans.
442*	440	Oa-M2-Ob bend + Oc,e *z*-trans. + Od *xy*-trans.
527*	540	T-O_{br}-T *xy*-bend
583*	568	M2 *xy*-trans. + T *z*-trans.
583*	573	Od,e *xy*-trans. + T *y*-trans. + K *xy*-trans.
638	659	O_{nb} *yz*-trans. + O_{br} -*yz*-trans.
703	702	O_{nb} *z*-trans. + O_{br} -*z*-trans. + M2-Ob stretch
754	754	Oa-M2-Ob bend
800*	820	T-Oc,d-T bend
811*	836	T-Oc,e-T bend
913	888	Tetrahedral breathing
958	970	T-O_{nb} stretch (ν_1)
1024	1023	T-O_{nb} stretch (ν_1) + O_{br} in/out tetr. base center
1098	1097	T1,2-Oc,e *xy*-stretch (ν_{10})
1116	1118	T1,2-Oc,d *xy*-stretch (ν_{10})

* Indicates weak observed modes whose frequencies were dictated by the calculations; observed frequency uncertainties are up to 10 cm^{-1}.

TABLE 4. Raman-active B_g $z(y,x)\bar{z}$ mode frequencies and assignments for muscovite

Observed (cm^{-1})	Calculated (cm^{-1})	Assignment
–	1	OH *xz*-trans.
–	17	sheet + K *y*-trans. shearing M2 environment
–	36	OH-M2-OH bend
101	99	sheet *xz*-trans. +K *y*-trans. (minor)
124	115	K *z*-trans. + tetrahedral rot. || *z*
124	130	sheet *xz*-trans. + K *y*-trans.
173	169	M2-OH stretch + T2 *x*-trans.
199	194	M2-OH stretch
217	219	OH *xz*-trans. + Ob *y*-trans. + Od *z*-trans.
265	268	K *y*-trans. + Oa,OH *x*-trans. + Oc,e *z*-trans.
265	274	T1-Oa *z*-trans. + T2-Ob –*z*-trans. + M2 *xy*-trans.
313	315	M2-OH stretch + M2-Ob stretch + K *y*-trans.
359*	353	M2 *xy*-trans. + OH *z*-trans. + Od -*xz*-trans. + K *yz*-trans.
382*	389	Oc,e *z*-trans. + M2 *z*-trans. + K *yz*-trans.
410	405	Obr *yz*-trans. + K *yz*-trans.
491	489	K *z*-trans. + tetrahedral rot. || *z* + M2-O_{nb} stretch
542*	536	T-O_{br}-T *xy*-bend
576*	568	M2 *xz*-trans. + T *z*-trans.
576*	578	Od,e *x*-trans. + T -*x*-trans. + K *y*-trans.
669*	667	O_{nb} *xz*-trans. + Oc,e *z*-trans.
704	716	O_{nb} *z*-trans. + O_{br} –*z*-trans.
754	754	Oa-M2-Ob bend
804*	816	T-Oc,d-T bend
851	839	T-Oc,e-T bend
912	888	Tetrahedral breathing
954	971	T-O_{nb} stretch (ν_1)
1017	1023	T-O_{nb} stretch (ν_{10}) + O_{br} in/out tetr. base center
1098	1097	T2-O, e stretch (ν_{10})
1116	1118	T2-Od stretch (ν_{10})

* Conventions in Table 3 apply.

provided guidelines for selecting weak Raman spectral features as fundamentals. During the initial stage of the fitting, it was not obvious to assign Raman-active fundamentals to certain weak Raman features, but as the calculations generated fundamental mode frequencies, we assigned some of these observed weak features to fundamental modes. The observed frequencies of the weak modes are not determined as confidently as those for the stronger modes and are uncertain up to approximately 10 cm^{-1} from the values listed in Tables 3 and 4. Due to the lack of polarization dependence for many weak Raman spectral features, we could not determine from the spectra whether each weak mode is A_g or B_g, but allowed the theory to make those assignments. These calculation-influenced observed mode assignments are indicated in Tables 3 and 4.

The total number of Raman-active fundamental modes predicted by FGA for the muscovite structure (57) is consider-

TABLE 5. IR-active A_u calculated mode frequencies and assignments for muscovite

Observed* (cm^{-1})	Calculated (cm^{-1})	Assignment
–	1	OH *xy*-trans.
–	51	sheet *z*-trans.
–	68	M2,OH,sheet *yz*-trans.: shearing K environment
108	107	M2, OH *yz*-trans. + Ob *y*-trans. + Od *yz*-trans. + K *x*-trans. (minor)
122	127	M2,OH *xy*-trans. + T2-Ob *yz*-trans. + Oe *yz*-trans.
188	180	OH-M2-OH bend + Od *xz*-trans.
–	218	K *x*-trans. + OH-M2-OH bend + Oa *x*-trans.
245	257	Oa,b *y*-trans. + OH *yz*-trans. (minor)
262	277	M2-OH *xz*-stretch + Ob *z*-trans. + Ob *y*-trans.
290	300	M2-OH *yz*-stretch + tetrahedral rot. & trans. || *z*
–	313	Oc *yz*-trans. + Ob *yz*-trans. + Oa *y*-trans. + K *x*-trans.
352	344	T1,Od,e *z*-trans. + T2,Oc –*z*-trans. + M2,OH *xy*-trans.
410	400	O_{br} *yz*-trans. K *x*-trans.
430	434	M2-Oa stretch + T1-Oa *z*-trans. + T2-Ob -*z*-trans.
475	483	M2 *z*-trans. + K-O_{nb} stretch
536	539	T-O-T *xy*-bend
549	574	O(d,e) *xy*-trans. + T *y*-trans. + K *xy*-trans.
697	707	O_{nb} *z*-trans. + O_{br} -*z*-trans. + M2 *z*-trans. (minor)
728	713	M2 *xy*-trans.: M2-Oa,b stretch
805	816	T-Oc,d-T bend
825	824	M2 *x*-trans.: M2-Oa,b stretch
–	835	T-Oc,e-T bend
–	866	Tetrahedral breathing
1003	981	T-O_{nb} stretch (ν_1)
1027	1017	T-O_{nb} stretch (ν_1) + O_{br} in/out tetr. base center
1062	1097	T-Oc,e stretch (ν_{10})
–	1118	T-Oc,d stretch (ν_{10})

* From Velde (1978).

TABLE 6. IR-active B_u observed and calculated mode frequencies and assignments for muscovite

Observed* (cm^{-1})	Calculated (cm^{-1})	Assignment
–	1	OH *xz*-trans.
–	58	sheet,M2,OH *x*-trans.: shearing K environment
–	109	K *yz*-trans. + tetrahedral rot. || *z*
122	124	M2-OH *xy*-trans. + Oc,d -*xy*-trans.
137	140	K *yz*-trans. + Oa *x*-trans. + Oc *z*-trans. + Od -*z*-trans.
165	181	OH-M2-OH bend + Od *xz*-trans.
188	203	K *y*-trans. + Ob -*y*-trans. + Oe *z*-trans. + OH *xz*-trans.
245	257	OH-M2-OH *xz*-bend + Ob *xy*-trans.
262	272	K *y*-trans. + O_{nb} *xy*-trans. + Oc *z*-trans. + Oe -*z*-trans.
290	316	OH-M2-OH *xy*-bend. + K *xz*-trans.
352	352	K *xy*-trans. + M2 *yz*-trans. + Oe *z*-trans. + Oc,d -*z*-trans.
–	370	M2 *z*-trans. + Od,e,K -*z*-trans.
410	405	Oc,e *z*-trans. + Od -*z*-trans. + K *z*-trans. (minor)
–	434	T1 *z*-trans. + T2 -*z*-trans. + Oa-M2-Ob bend
–	527	M2,K *z*-trans. + T -*z*-trans. + Od *x*-trans.
536	538	Od,e *y*-trans. + T1 *y*-trans. T2 -*y*-trans.
549	577	T1 *x*-trans. + T2 -*x*-trans. + Oc *y*-trans.
697	713	M2-Ob *xy*-stretch + Oa *y*-trans.
728	723	O_{nb} *z*-trans. + O_{br} -*z*-trans.
805	814	T-Oc,d-T bend
825	823	M2 *x*-trans.: M2-Oa,b stretch
–	839	T-Oc,e-T bend
–	866	Tetrahedral breathing
1003	981	T-O_{nb} stretch (ν_1)
1027	1017	T-O_{nb} stretch (ν_1) + O_{br} in/out tetr. base center
1062	1097	T-Oc,e stretch (ν_{10})
–	1118	T-Oc,d stretch (ν_{10})

* From Velde (1978).

ably larger than the number of features (20) clearly observed in the Raman spectra that call be assigned to fundamental modes (Fig. 2). These differences can be explained by several factors, the most important of which is the the scant polarization dependence for most spectral features. This weak polarization dependence is seen in the spectra reported for green muscovite by Loh (1973), and in the theory, where many calculated A_g and B_g mode pairs are at similar or identical frequencies. The data and calculations indicate that 14 spectral features can be assigned to both A_g and B_g species; one peak in both Raman spectra can be assigned to four modes, two each for A_g and B_g. Variations between the A_g and B_{5g} spectra are subtle, where most differences (slight intensity differences, and peak shifts or shape changes) are seen for the lower frequency modes. The calculations placed four modes at frequencies lower than the 85 cm^{-1} laser line filter cut off in the FT Raman spectra. Some of the broad fea-

tures in the spectra could be assigned to more than one A_g or B_g mode by the calculations, which could reasonably fit 53 of the 57 calculated Raman mode frequencies to the target frequencies determined from the spectra.

The calculated frequency and the associated atomic motion (eigenvector) for each Raman-active mode is listed in Tables 3 through 4. Calculated frequencies and mode assignments for the IR-active A_u and B_u species are presented for completeness in Tables 5 and 6, respectively. Normal mode frequencies and eigenvectors were also calculated for the isolated tetrahedral sheets by gradually varying to zero all force constants involved with the K and M2 environments.

DISCUSSION

Force constant values

The force constant values determined for muscovite (Table 2) are generally similar to those found for phlogopite, reconfirming force constant transferability between cyclosilicates and sheet silicates (McKeown et al. 1999). The T-O_{nb}, T-O_{br}, M2-O, M2-OH, and K-O values calculated for muscovite are within 15% of those determined for phlogopite. The magnitude of the T-O_{br} and T-O_{nb} values for muscovite are reversed with respect to equivalent force constants for phlogopite. Larger differences are found between equivalent sets of bond bending force constants for the two structures. The O_{br}-T-O_{br} value falls within the range of those determined in our earlier work on other silicate structures, while the O_{nb}-T-O_{br} value is the smallest of those determined earlier, but is less than 10% lower than that calculated for beryl (Kim et al. 1995). The magnitude reversal of force constants between muscovite and phlogopite are also seen for the O_{nb}-T-O_{br} and O_{br}-T-O_{br} values.

We cannot be sure about the cause behind the magnitude reversals seen for the force constants describing the T, O_{nb}, and O_{br} environments between muscovite and phlogopite, but these trends may be related to the symmetry of the associated tetrahedral rings. Between muscovite and phlogopite the lower symmetry structure appears to generally favor higher force constant values for the O_{br} bonding environments. For six-membered tetrahedral rings, this trend is found for the O-Si-O bond bending environments within dioptase (lower ring symmetry) (McKeown et al. 1995) vs. equivalent environments in beryl (higher ring symmetry).

Frequencies of calculated modes vs. observed Raman- and IR-active fundamental modes

Calculated fundamental mode frequencies were fit to observed mode frequencies determined from the features in the two polarized Raman spectra so that eigenmodes are assigned to virtually all peaks in the data (Fig. 2). Intensity and frequency differences of features between both spectra are subtle; as a consequence of this, assignment of A_g and B_g modes to features common to both spectra was done for peaks at or near 124, 172, 198, 217, 265, 316, 382, 411, 703, 754, 800, 913, and 958 cm^{-1} in both spectra. Above 1000 cm^{-1}, A_g and B_g modes were assigned to the broad features near 1024, 1098 cm^{-1}, and 1116 cm^{-1}, where observed frequency determinations of modes were somewhat subjective; the 1116 cm^{-1} peak has a broad lower frequency shoulder that includes the 1098 mode and extends to the 1024 cm^{-1} peak. The calculations generated pairs of modes that have similar frequencies; from this, an A_g mode pair was assigned to the 583 cm^{-1} peak and a B_g mode pair was assigned to the 576 cm^{-1} peak. A_g and B_g mode pairs were assigned to the 265 cm^{-1} peak in both spectra. No assignments were made to what appear to be the lowest frequency peaks in the Raman spectra near 43 and 85 cm^{-1}, because these features are below the laser line filter cut-off. Intensity changes of these lowest frequency features from A_g to B_g are due to the change in the relative intensity of the Rayleigh line, which is typically larger for the parallel polarized A_g spectrum than the cross polarized B_g spectrum.

No observed IR fundamental mode frequencies were used in the fitting process; however, the calculated A_u and B_u mode frequencies (Tables 5 and 6) are compared with the IR data presented for muscovite by Velde (1978) and Loh (1973). To our knowledge, Velde presents the most extensive list of observed IR mode frequencies; however, there is no indication of which modes have A_u or B_u symmetry. These frequencies are listed in Tables 5 and 6 for detailed comparisons and are arranged so that closest matches are made with our calculated A_u or B_u mode frequencies. In general, most major peaks in the IR data appear to correspond to groups of calculated IR modes. Calculated A_u modes at 344, 400, 483, 539, 574, 981, 1017, 1097, and 1118 cm^{-1}, as well as calculated B_u modes at 352, 370, 405, 434, 527, 538, 577, 981, 1017, 1097, and 1118 cm^{-1} can be assigned to the two broad and intense bands in the IR spectra: from 350 to 620 cm^{-1} and from 980 to 1100 cm^{-1} (see Velde 1978 Fig. 1). The calculated 707, 713. 816, 824, and 835 cm^{-1} A_u modes as well as the calculated 713, 723, 814, 823, and 839 cm^{-1} B_u modes appear to correspond to the cluster of peaks centered near 750 cm^{-1}, between the broad bands in the IR spectra.

Eigenmode descriptions and assignments

Eigenmodes for all vibrational species can be grouped into three frequency ranges according to dominant atomic displacements. Internal sheet modes dominate at frequencies greater than 800 cm^{-1} and are the localized T-O stretch and T-O-T bending motions. Modes at frequencies between 800 and 360 cm^{-1} contain mixtures of K and M2 site motions with displacements internal to the tetrahedral sheets. At frequencies below 350 cm^{-1}, lattice modes dominate where M2, K, and OH motions mix with whole sheet displacements.

Displacements calculated within the linked six-membered rings in muscovite are generally different with respect to those found earlier for the isolated six-membered rings in beryl and dioptase (Kim et al. 1995; McKeown et al. 1995). Where motions are similar to those found for the rings in cyclosilicate crystals, ν_n symbols are used. However, these symbols can only be used to describe the highest frequency, most localized eigenmodes for muscovite (Tables 3 through 6) where n is either 1 or 10 (McKeown et al. 1993).

The localized, internal sheet eigenmodes above 800 cm^{-1} are similar for all species, where a general pattern is followed from the highest frequencies: ν_{10} (T-O_{br} stretch, Fig. 3a left), ν_1 (T-O_{nb} stretch), tetrahedral breathing, and T-O-T bending. This is in contrast to phlogopite where A_g-B_u and B_g-A_u eigenmode pairs share similar atomic displacements. The tetrahedral breathing modes near 880 cm^{-1} for all species have O atoms moving toward the T site in one tetrahedron, and O atoms in the three

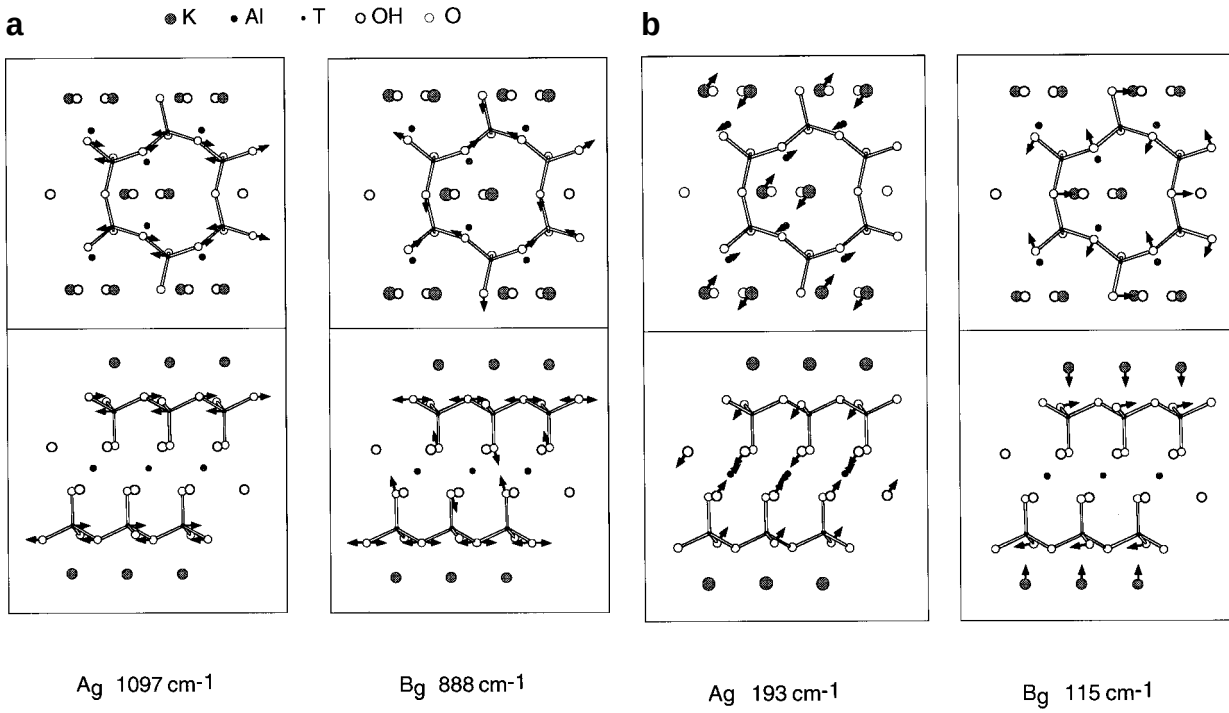

FIGURE 3. (a) Calculated atomic motions for the normal modes internal to the silicate sheets in the muscovite structure. The diagrams in the upper and lower boxes are the *z* axis and the *y* axis projections, respectively. In the *z* axis projection, only the top silicate sheet of the two in the cell is drawn for clarity. Arrows are drawn to scale, indicating the relative amplitude of the motion of each atom in each normal mode. **(b)** Examples of the muscovite lattice vibrational modes. The conventions in **a** apply.

neighboring tetrahedra moving away from the T sites (Fig. 3a right). For the IR modes, M2-O stretch motion is mixed with two T-O-T modes near 820 cm^{-1}.

Many of the intermediate frequency modes are dominated by O-M2-O bend, as well as M2-O and K-O stretch motions that mix with internal sheet displacements. Below 600 cm^{-1}, K motions are present in several of these eigenmodes and continue to be found in many of the lattice modes.

Lattice modes have motions from all atom types in the muscovite structure; many lattice modes contain OH displacements. At frequencies lower than 150 cm^{-1}, whole sheet motions mix with K or M2 displacements. An interesting set of modes found for all vibrational species can be described as tetrahedral rotation about an axis perpendicular to the sheets that is driven by K *z*-translations (Fig. 3b right), where the sense of rotation of each tetrahedron alternates around the ring in clockwise and counter-clockwise directions. An exception to this is the B_g mode at 491 cm^{-1} where the tetrahedral rotations are mixed with M2-O stretch. This mode can be described as O_{br} breathing, where half of a six-membered ring's bridging O atoms are translating into the ring center and the other half are translating away. Lattice modes can have sheet displacements along the *c* or *z* directions, where the M2 or K environments are compressed or expanded (Fig. 3b left). A set of low frequency modes, one each for all vibrational species, has the sheets and the K or M2 environments move in similar directions to create a shearing action around the M2 or K sites, respectively. Shearing around M2 is found for the Raman-active modes and around K for the IR-active modes.

Similar to our conclusions made for phlogopite, specific eigenmode assignments made to Raman and IR modes in this study do not agree particularly well with assignments made by Loh (1973). The discrepancies are likely due to the fact that Loh made vibrational assignments based on the MO_6 octahedral and TO_4 tetrahedral symmetry of atom clusters in muscovite and observations of Raman modes from similar atom clusters in other materials, whereas the eigenmodes calculated here are based on the muscovite structure. Loh's general arguments agree to some extent with our findings, but as in the phlogopite study, many discrepancies are seen in the details. According to Loh, Raman modes at frequencies greater than 300 cm^{-1} are dominated by T-O stretch motions within the tetrahedra. This argument is partially supported by our findings, but Raman-active eigenmodes in this frequency range can have dominant M2 as well as K displacements mixed with internal sheet motions. According to Loh, MO_6 octahedral modes dominate at frequencies less than 200 cm^{-1}. We find that eigenmodes in this frequency range can contain octahedral motions mixed with lattice-like OH and sheet displacements.

Vibrational mode assignments made by Velde (1978) to features in the IR spectra are more consistent with the IR-active eigenmodes calculated for the muscovite structure. According to Velde, the broad band near 1062 cm^{-1} is due to Si-apical oxygen stretch ($Si\text{-}O_{nb}$); this is in partial agreement with the

eigenmodes, where both Si-O_{nb} and Si-O_{br} stretch modes occur near this frequency. Velde assigned tetrahedral Al-O-Al, Al-O-Si, and O-Si-O bend modes to peaks near 825, 805, and 536 cm^{-1}, respectively, that are generally consistent with eigenmodes calculated near these frequencies. Velde also assigned K motion to the low frequency 137 and 122 cm^{-1} modes, where eigenmodes in this frequency range have K and M2 motion. M2-OH and OH motions are assigned to peaks near 912 and 620 cm^{-1} by Velde, whereas eigenmodes having OH displacements are calculated at frequencies only as high as 340 cm^{-1}.

Far IR measurements (Tateyama et al. 1977) show modes at 106, 164, and 188 cm^{-1} for muscovite. Calculated A_u modes at 107 and 180 cm^{-1} as well as B_u modes at 109, 181, and 203 cm^{-1} are the closest matches to these observations. Tateyama et al. assigned K-O stretch motion to the 106 cm^{-1} mode that is consistent with the 109 cm^{-1} B_u eigenmode having K translations. Eigenmodes calculated in this low frequency range are not completely dominated by K-O stretch motions as Tateyama suggests, but also contain M2, OH, and sheet motions.

Frequency vs. inter-sheet coupling relationships

All force constants not involving the T sites were gradually reduced to zero to vibrationally isolate the tetrahedral sheets in muscovite. This was done by introducing a scale factor α where $0 \le \alpha \le 1$, to all force constants involving K and M2 sites (i.e., k_i, where i = 3, 4, 5, and 8 in Table 2) (Kim et al. 1995). The frequency vs. α relationships for all four vibrational species of muscovite are similar; this is different behavior with respect to phlogopite, where pairs of species, A_g-B_u and B_g-A_u, have similar relationships.

Internal sheet, mixed (internal sheet, K, and M2 displacements), and lattice modes each exhibit distinctive behavior as α is varied from one (crystal structure) to zero (isolated tetrahedral sheet); the determination of these eigenmode groups described above was done in part from these relationships. Frequencies of the internal sheet modes do not vary much and no character exchanges of modes are observed. As α is varied to zero, the intermediate frequency mixed modes exchange character and generally drop rapidly in frequency as M2 and K contributions drop out of the eigenmodes. Lattice mode frequencies approach zero as α approaches zero. These relationships indicate that the bonding strength between the sheets in the muscovite structure is large enough to affect eigenmodes at frequencies as high as 824 cm^{-1}, where M2 displacements are first observed. For phlogopite, these effects can be seen in eigenmodes as high as 880 cm^{-1}.

ACKNOWLEDGMENTS

We thank J.E. Post and P. Pohwat (Mineral Sciences Department, National Museum of Natural History, Smithsonian Institution) for the muscovite sample. We also thank R.J. Hemley and A. Goncharov (Geophysical Laboratory) for access to their micro-Raman facility and help with collection of the preliminary data. This work was supported, in part, by the U.S. Army Waterways Experiment Station and the Office of Naval Research. Certain commercial equipment, instruments, or materials are identified to specify experimental procedures. Such identification does not imply recommendation by the National Institute of Standards and Technology, nor does it imply that the materials or equipment identified are necessarily the best available for the purpose.

REFERENCES CITED

Fateley, W.G., Dollish, F.R., McDevitt, N.T., and Bentley, F.F. (1972) Infrared and Raman Selection Rules for Molecular and Lattice Vibrations: the Correlation Method. Wiley, New York.

Guven, N. (1971) The crystal structures of $2M_1$ phengite and $2M_1$ muscovite. Zeitschrift für Kristallographie 134, 196–212.

Haley, L.V., Wylie, I.W., and Koningstein, J.A. (1982) An investigation of the lattice and interlayer water vibrational spectral regions of muscovite and vermiculite using Raman microscopy. Journal of Raman Spectroscopy, 13, 203–205.

Kim, C.C., Bell, M.I., and McKeown, D.A. (1993) Vibrational analysis of benitoite and the Si_3O_9 ring. Physical Review, B47, 7869–7877.

———(1995) Vibrational analysis of beryl and the Si_6O_{18} ring. Physica B, 205, 193–208.

Loh, B. (1973) Optical vibrations in sheet silicates. Journal of Physics C: Solid State Physics, 6, 1091–1104.

Loudon, R. (1964) Raman scattering from crystals. Advances in Physics, 13, 423–482.

McKeown, D.A., Bell, M.I., and Kim, C.C. (1993) Raman spectroscopy of silicate rings: benitoite and the three-membered ring. Physical Review B, 48, 16357–16365.

———(1995) Vibrational analysis of dioptase and its puckered six-membered ring. Physics and Chemistry of Minerals, 22, 137–144.

McKeown, D.A., Bell, M.I., and Etz, E.S. (1999) Vibrational analysis of the trioctahedral mica: phlogopite. American Mineralogist, in press.

Tateyama, H., Shimoda, S., and Sudo, T. (1977) Estimation of K-O distance and tetrahedral rotation angle of K-micas from far-infrared absorption spectral data. American Mineralogist, 62, 534–539.

Velde, B. (1978) Infrared spectra of synthetic micas in the series muscovite-MgAl celadonite. American Mineralogist, 63, 343–349.

MANUSCRIPT RECEIVED NOVERMBER 3, 1998
MANUSCRIPT ACCEPTED FEBRUARY 24, 1999
PAPER HANDLED BY HANS KEPPLER